Applied Surface Science 735 (2026) 166674

Contents lists available at ScienceDirect

Applied Surface Science

journal homepage: www.elsevier.com/locate/apsusc

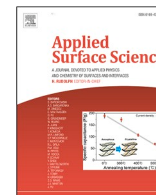

Full Length Article

Electrode-Modulated oxygen defect profiles in intentionally oxidized chalcogenide ovonic threshold switch selectors

MiRiNae Lee [a,b], Jung Hoon Han [a,c], Chahwan Yang [a,b], Kyunghee Choi [a,*], Sooji Nam [a,b,*]

[a] Reality Devices Research Division, Electronics and Telecommunications Research Institute, 218, Gajeong-ro, Yuseong-gu, Daejeon, the Republic of Korea
[b] Semiconductor and Advanced Device Engineering, University of Science and Technology, 217, Gajeong-ro, Yuseong-gu, Daejeon, the Republic of Korea
[c] Department of Micro/Nano System, Korea University, 145, Anam-ro, Seongbuk-gu, Seoul, the Republic of Korea

ARTICLE INFO

Keywords:
Oxidized Ovonic Threshold Switch
Selector
Via-hole type

ABSTRACT

In the push for next-generation memory technologies, crossbar selector devices play a critical role in suppressing sneak-path currents and enabling three-dimensional integration. This study investigates the operation of ovonic threshold switch devices based on Se-alloyed TeO_x, focusing on how interfacial oxidation and electrode materials influence the switching behavior. A small amount of oxygen was intentionally incorporated during the deposition step, enabling stable selector operation without the need for additional dopants. Devices fabricated with Pt, W and Cr electrodes exhibited threshold switching with sub-50 ns responses and selectivity exceeding 10^3, with Pt delivering the best endurance (>10^3 cycles). In contrast, Ti, Ni and Al electrodes formed interfacial oxide layers, as confirmed by cross-sectional transmission electron microscopy, energy-dispersive X-ray spectroscopy, and electron energy loss spectroscopy, leading to resistive random-access memory-like behavior or switching failures. Optimal performance was consistently observed at a specific Se sputtering power (10 W), corresponding to low areal density and improved film uniformity, as verified by X-ray photoelectron spectroscopy, Rutherford backscattering spectrometry, atomic force microscopy, and Raman spectroscopy. These findings demonstrate that selector performance capabilities are governed not only by the active-layer composition but also by electrode-induced interfacial defects. This work offers concrete design guidelines for reliable, low-voltage selector integration in future high-density memory architectures.

1. Introduction

With the rapid expansion of the artificial intelligence industry, deep-learning workloads demand ever-larger data repositories [1]. In relation to this, global amounts of stored data are projected to reach 175 zettabytes (1 ZB = 10^{21} Bytes) by 2025 [2]. In addition, the general power usage effectiveness (PUE) of data centers for the storage of 175 ZB of information and for AI learning has been estimated as 1.55 according to industry report [3,4]. PUE is defined as the ratio of the total power input to a data center to the power consumed by its IT equipment; a value above 1 signifies that the excess is used for auxiliary systems such as cooling. It can be inferred that more than half of the power consumed by silicon-based devices is devoted to cooling. Consequently, hyperscale data centers—where silicon-based memory and logic dominate—now account for an estimated 1–3% of worldwide electricity consumption due to their high-power demand and cooling requirements [5,6].

Silicon, due to its indirect bandgap and material properties, dissipates a significant portion of carrier energy as heat rather than converting it efficiently into electrical work, leading to increased thermal losses. Excess heat in densely integrated silicon devices induces thermal hotspots and steep temperature gradients, amplifying leakage currents and electromigration These thermal constraints limit device scaling and 3D integration [7,8]. Moreover, the mechanical and structural limitations of silicon, such as junction leakages and dielectric breakdowns under high electric fields, pose challenges that hinder further device miniaturization efforts [9–12]. To transcend silicon's thermal and scaling limitations [13–15], alternative materials and architectures are urgently sought. One promising candidate is the chalcogenide ovonic threshold switch (OTS), whose field-driven mechanism enables nanosecond-scale switching and low power dissipation, thereby facilitating dense three-dimensional integration [16,17].

OTSs are nonlinear resistive elements based on an amorphous chalcogenide material. They exhibit volatile switching behavior according to which the resistance decreases abruptly when a defined threshold

* Corresponding authors.
E-mail addresses: kyunghee.choi@etri.re.kr (K. Choi), sjnam15@etri.re.kr (S. Nam).

https://doi.org/10.1016/j.apsusc.2026.166674
Received 3 December 2025; Received in revised form 11 March 2026; Accepted 20 March 2026
Available online 22 March 2026
0169-4332/© 2026 The Authors. Published by Elsevier B.V. This is an open access article under the CC BY license (http://creativecommons.org/licenses/by/4.0/).

voltage is exceeded. These devices serve as selectors that mitigate sneak currents in crossbar memory arrays. For selector applications, the material must remain amorphous while withstanding high-temperature annealing during the back-end-of-line process.

Existing studies have explored multicomponent OTS systems containing more than four elements [18], with examples being Ge–Te–Si–N–C [19], Ge–Te–C–N [20], Ge–Te–As–Si–N [21] and Ge–Te–As–Se–Si [22]. These systems demonstrate stable performance with selectivity (I_{on}/I_{off}) exceeding 10^4 and threshold voltages V_{th} of less than 2 V. Research on such multicomponent OTS materials continues.

In the present study, stable device operation is pursued by doping a small amount of oxygen into otherwise pure chalcogen-based OTSs, in contrast to the conventional multicomponent chalcogenide OTS. Importantly, oxygen doping in chalcogenide films induces O–VTe–Ge dumbbell-like defects, raising the crystallization temperature and stabilizing the amorphous phase. This retards the crystallization kinetics and enhances thermal stability [23,24]. In previous studies, Ge, As, Si, C and N, among other elements, were added to raise the crystallization temperature and stabilize the amorphous system [25]. However, introducing these elements requires an additional material source in the deposition tool, and for a multicomponent system, there are numerous parameters that must be optimized to achieve the desired composition, which demands a significant amount of time. We thus benefit from reducing the composition optimization time by simply oxidizing the active-layer in a Te–Se binary system. Oxygen doping offers the major advantage of conferring similar benefits while being controllable at the process-design stage without the need for a separate material, although it also increases the risk of partial oxidation at the electrode interface.

Nevertheless, the impact of such “intentional oxidation”—which forms a new defect-state/oxide layer at the electrode–OTS boundary—has not yet been sufficiently investigated. Existing studies regard chalcogenide-based OTSs as non-oxidizing and attribute electrode-dependent behavior to the interfacial defect density: a higher defect density lowers the barrier between trap sites via the Poole–Frenkel effect [26,27].

In contrast, this study directly visualizes interfacial oxidation and related defects through transmission electron microscopy (TEM), energy-dispersive X-ray spectroscopy (EDS), electron energy loss spectroscopy (EELS), X-ray photoelectron spectroscopy (XPS), and Raman analyses of devices fabricated with a via-hole structure (Fig. 1a–b), experimentally demonstrating that the device-switching characteristics vary with the electrode-specific defect profiles, in contrast to previous studies, which relied on physical models that deduced defects solely from electrical data. This work clarifies the interplay between the electrode and the oxidized OTS interface through direct structural and chemical analyses.

2. Experimental Section

In the MIM structure, the bottom electrode was fabricated on a 100-nm-thick SiO_2 layer on a silicon substrate. First, 100 nm of TiW(10% Ti, 90% W) was deposited by DC sputtering and patterned to form the bottom electrode. Thereafter, a 100 nm SiO_2 layer was deposited at 300 °C via PECVD (P5000 Mark II, AMAT) and patterned to create measurement contact holes and selector vias. Next, the active-layer pattern under four power conditions [Se: 0, 10, 20 or 30 W and Te: 40 W] was deposited at room temperature by DC co-sputtering through a shadow mask in an Ar:O_2 (20:2 sccm) gas mixture. The top electrode was patterned with the same shadow mask, and Pt, Cr, Ti, Ni and Al were deposited by electron-beam evaporation. The tungsten (W) target was sputtered under identical shadow-mask conditions. The thickness of the top electrode was 100 nm. Standard photolithography was employed for all electrode and via patterning steps.

The absorption coefficient of the active-layer under four conditions was measured by UV–Vis spectroscopy (transmission and absorbance) (Lambda 1050, Perkin Elmer). Horizontal sections of the linear region in the tauc plot were extracted for each film. Additionally, UPS measurements (He Iα, 21.2 eV) for each thin-film condition were taken (Nexsa G2, Thermo Scientific). The film density and elemental composition were assessed by XPS depth profiling (Nexsa G2, Thermo Scientific) and RBS (6SDH-Q, NEC). To visualize the interfacial oxidation, high resolution-TEM imaging was conducted (JEM-F200, JEOL), and the oxygen distribution at the active-layer–top-electrode interface was evaluated by collecting the spectra via EDS (JEM-F200, JEOL) and EELS (Spectra Ultra, Thermo Fisher).

I–V characteristics were measured to evaluate the selector selectivity characteristics and the threshold voltage. Measurements were conducted at room temperature in the dark using a semiconductor parameter analyzer. Here, V and I denote the applied voltage and measured current, respectively. For triangular-wave input measurements, a function generator and an oscilloscope were mounted within a light-tight enclosure to apply triangular waveform stimuli and to monitor the resulting current. Triangular waves of 5 V_{pp} at 800 kHz were applied.

3. Results and Discussion

3.1. Electrical characteristics

In Fig. 2, the current–voltage (I–V) characteristics for four active-layer conditions (Se 0–30 W) and six types of electrodes are summarized. Fig. 2a–f show that, under the Se 0 W condition, every electrode except Ti exhibits only leakage-level current or fully insulating behavior. However, the Ti electrode displays a transient resistive random-access memory (RRAM)-like current burst, as shown Fig. 2d. Overall, the Se

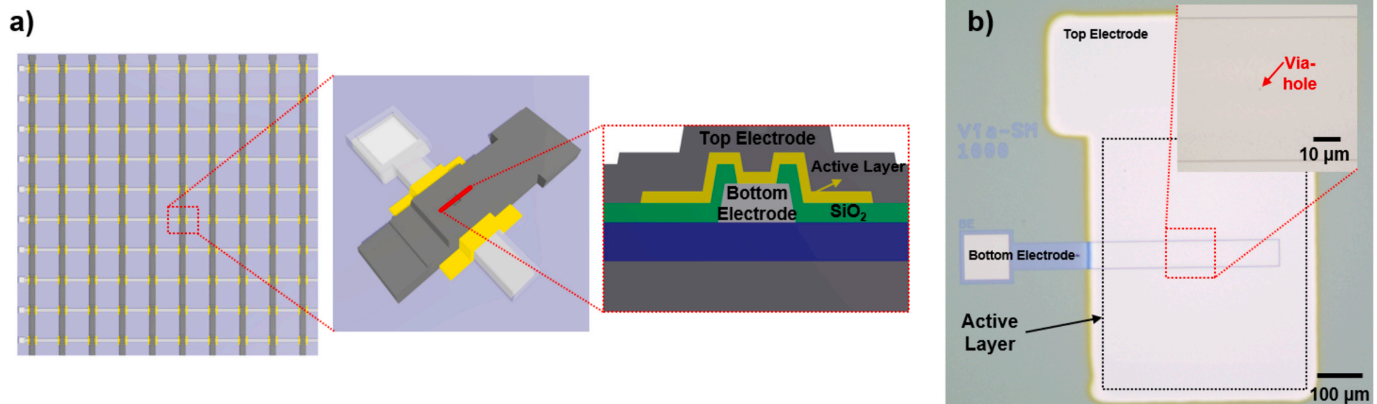

Fig. 1. A) array, single-device and cross-sectional views of a via-hole-type selector, with b) an om image confirming a hole size of ~ 1,000 nm.

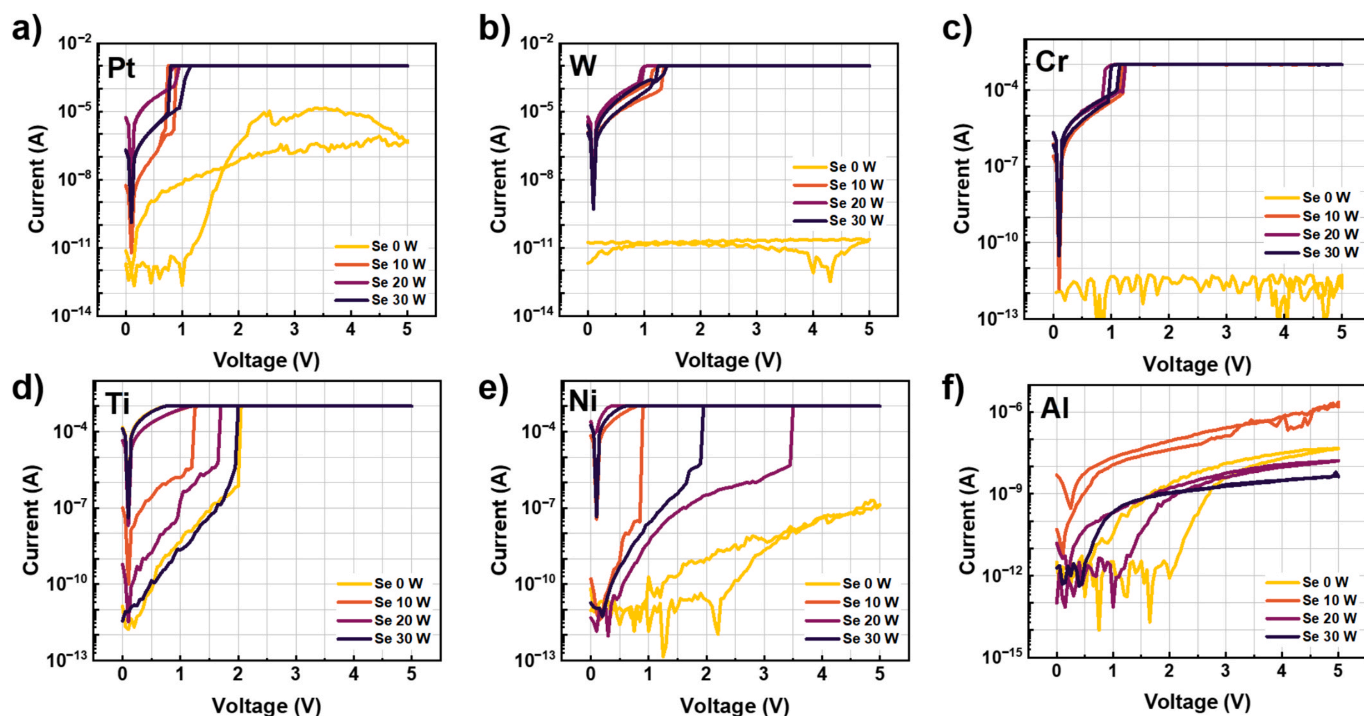

Fig. 2. Electrical characteristics of Se/TeO_x-based OTS selector devices using a) Pt, b) W, c) Cr, d) Ti, e) Ni and f) Al electrodes.

0 W active-layer behaves as an insulator that blocks current flow rather than as a semiconductor that supports conduction under specific bias condition. In contrast, Se-alloyed layers operate as effective selectors with Pt, W, and Cr electrodes. The Pt electrode delivers selectivity of $\approx 10^3$–10^4 (Fig. 2a) and endurance beyond 10^3 cycles. The W electrode shows slightly lower selectivity of $\approx 10^2$. Cr-electrode devices provide modest selectivity of 10–10^2. Across all electrodes that function as selectors, Se 10 W yields the best performance; every top-performing device reported herein employs this active-layer composition. Under the conditions where the electrodes operated successfully, we observed that the I-V characteristics varied with Se concentration. Specifically, a higher Se concentration led to a lower overall on/off ratio. This tendency is corroborated by Fig. S1 (Supporting Information). Overall, Pt affords the highest cycle count and, on average, the greatest selectivity. The anomalous behavior of the Al electrode is attributed to the formation of a thick interfacial Al_2O_3 layer that suppresses selector operation by introducing a large parasitic voltage drop [28].

Fig. 3a–c further confirm sub-50 ns turn-on switching speeds for Pt, W and Cr, underscoring their suitability as selectors. For Ti and Ni electrodes, the I–V characteristics deviate from selector-type behavior

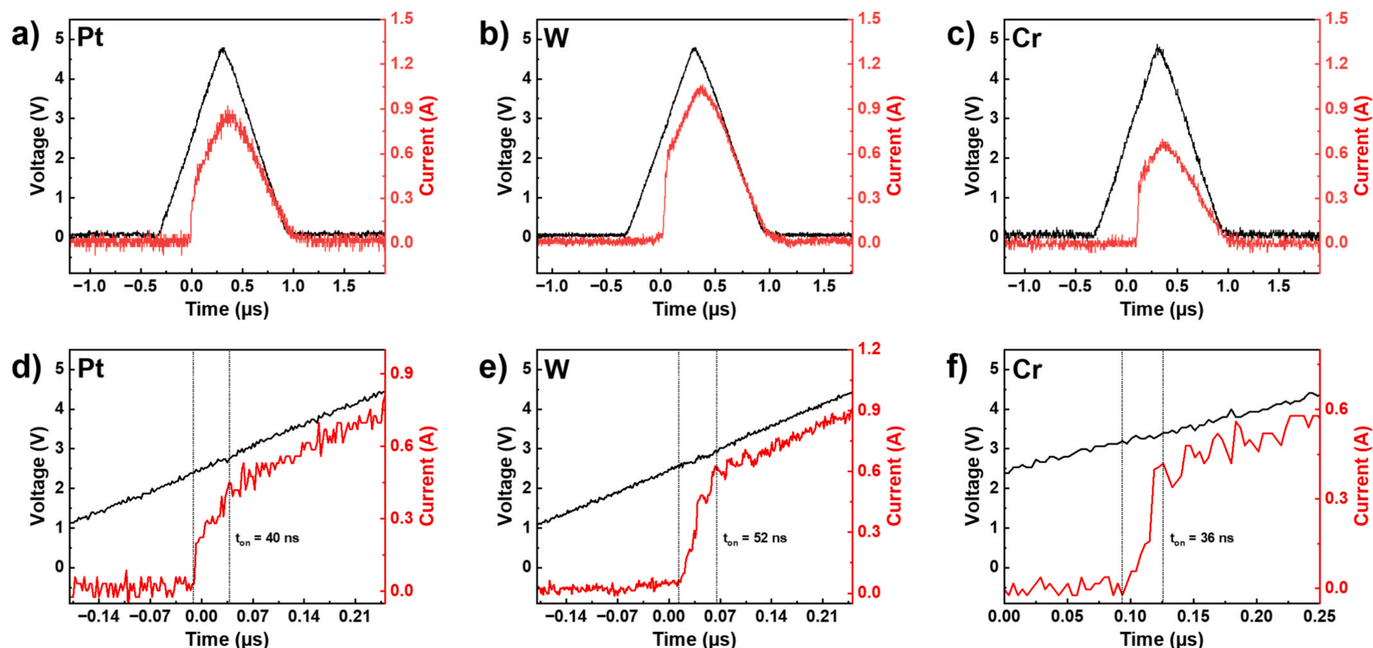

Fig. 3. A-c) triangular waveform measurements and d-f) turn-on speed graphs of se 10 W/TeO_x-based electrode OTS selector devices taken to assess the switching speed characteristics.

and instead exhibit RRAM-like responses, as evidenced by the absence of a discernible V_{hold} and the persistence of conduction after switching. Finally, with Al electrodes the current remains at leakage levels without abrupt resistance changes under any active-layer condition; as shown in Fig. S2 (Supporting Information), only under exceedingly high bias does an insulating-breakdown-like curve appear, and the device fails to operate as a selector. Due to these characteristics, the switching speed could not be observed in the Ti, Ni and Al cases. Fig. S3 (Supporting Information) confirms that no switching is observed when the active-layer does not contain oxygen, while the XRD data in Fig. S6 (Supporting Information) suggest that oxygen replaces Se–Se bonds [29], enhancing the amorphous characteristic.

When evaluating the endurance for each electrode, Pt showed the best performance with values exceeding 10^3 cycles, as shown in Fig. 4a. Although Cr and W did not reach this level, they exhibited measurable endurance outcomes nonetheless (Fig. 4b, c). However, unlike Cr, W demonstrated high selectivity but showed more pronounced degradation.

3.2. Hypothesis for selector operation

In Section 3.2, we present hypotheses that explain the device differences observed in Section 3.1 and present supporting experimental data. Because the selector has a canonical metal–insulator–metal (MIM) structure, its behavior is mainly governed by two transport mechanisms: bulk-limited [30–33] and electrode-limited [34–36] conduction. Section 3.2 therefore introduces these transport-based hypotheses and describes how these mechanisms relate to the electrical behavior reported above.

3.2.1. Hypothesis 1: Effects of composition and active-layer density differences

The first hypothesis suggests that differences in the composition and in the density of the active-layer influence device performance outcomes depending on the electrode. To test this hypothesis, Rutherford backscattering spectrometry (RBS) [37,38] was used to measure the density under each condition, with the peak intensities of the constituent elements also examined via XPS simultaneously to confirm the composition ratio [39,40]. Based on the density, composition ratio, and conductive-atomic force microscopy (C-AFM) results, it was possible to identify the active-layer conditions that led to optimal selector performance.

AFM illustrates the surface topography at high resolutions, revealing features such as surface roughness, grain boundaries and defect distributions. C-AFM, undertaken while applying bias to the probe, simultaneously acquires local current maps, enabling the identification of electrically active sites such as leakage pathways or conductive filaments [41]. In chalcogenide thin films, regions exhibiting higher current levels in C-AFM images often correlate with smoother or more well-defined morphological features. This correlation arises because electrical conduction tends to follow topographically continuous or less resistive regions, where structural disorder is relatively suppressed [42]. Consequently, areas with enhanced current contrast may also exhibit clearer or more uniform surface morphologies in AFM topography. The particle-like bright dots observed in Fig. 5a–d originate from intrinsic nm-scale compositional or density inhomogeneities in amorphous chalcogenide films, which locally alter the electrical transport pathways and manifest as localized conduction spots in the corresponding C-AFM images, rather than grain-boundary-related conduction [43,44].

AFM and C-AFM were employed to assess the degree of selector functionality for each active-layer condition. As shown in Fig. 5e, the Se 0 W condition did not support selector operation, as current flow appeared only at isolated spots and was absent over larger areas, regardless of the grain structure. In contrast, other conditions exhibited areal-scale conduction, especially Se 10 W (Fig. 5f), which showed more uniform instantaneous current flow, indicating superior selector behavior under this condition. It should be noted that C-AFM measurements do not directly demonstrate selector or OTS operation, but rather provide complementary information on the spatial distribution and microscopic nature of conduction paths within the active layer.

As evidence to support the C-AFM results discussed above, we employed XPS, RBS, and Raman spectroscopy to investigate the composition ratio, surface density and bonding state of each active-layer thin film.

In Fig. 6a, the Te content across active-layer conditions is analyzed, revealing a decrease in the Te content with an increase in the Se sputtering power. Notably, the amount of TeO_x remained relatively constant, while the amount of elemental Te decreased. This trend correlates with the increase in the Se peak intensity observed in Fig. 6c. Peak deconvolution in Fig. 6b, d was performed to identify the chemical states and peak positions. The XPS trends were consistent across the other conditions, as shown in Figs. S4, 5 (Supporting Information).

Additionally, the RBS results for the areal density, shown in Fig. 6e, were cross-validated with XPS, confirming consistent trends in the Te and Se concentrations. The combined areal density and composition ratios derived from XPS and RBS are summarized in Table 1. Among all conditions, Se 10 W exhibited the lowest areal density [45].

This trend was investigated further using Raman spectroscopy. As shown in Fig. 6f, for Se 0 W—without the addition of Se—the intensity of the Te bonding peak was high. However, beginning at Se 10 W, the peak intensity decreased sharply, suggesting the disruption of Te–Te symmetry bonds due to Se incorporation [46]. This leads to local reductions in the density, likely due to the formation of vacancies or the incorporation of Se atoms at the bonding sites. These Se-induced modifications suppress metallic Te–Te conduction and introduce trap states, thereby establishing a trap-assisted transport framework essential for threshold switching.

3.2.2. Hypothesis 2: Schottky junction according to work function differences

In the previous section, it was confirmed that the internal conduction of the active-layer thin film does not significantly affect the metal-

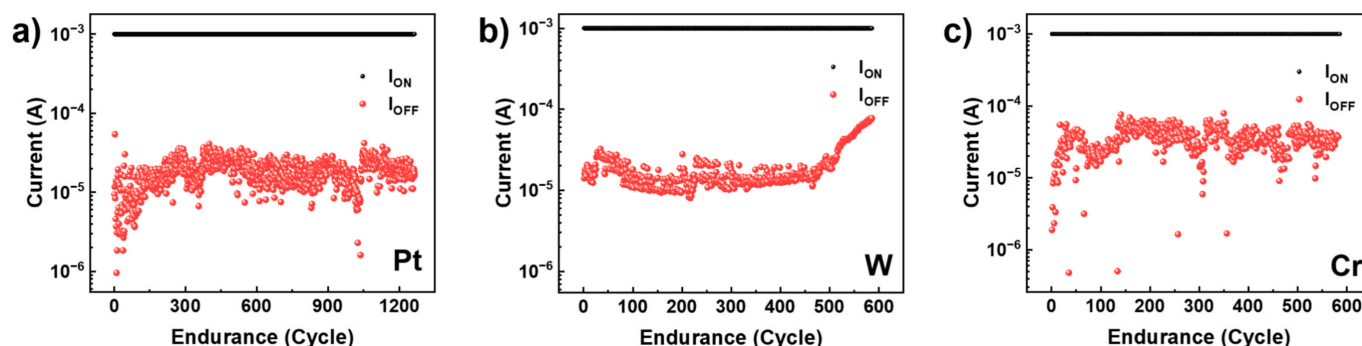

Fig. 4. On/off currents after repeat voltage vias up to the Se 10 W/TeO_x device limit using a) Pt, b) W and c) Cr electrodes.

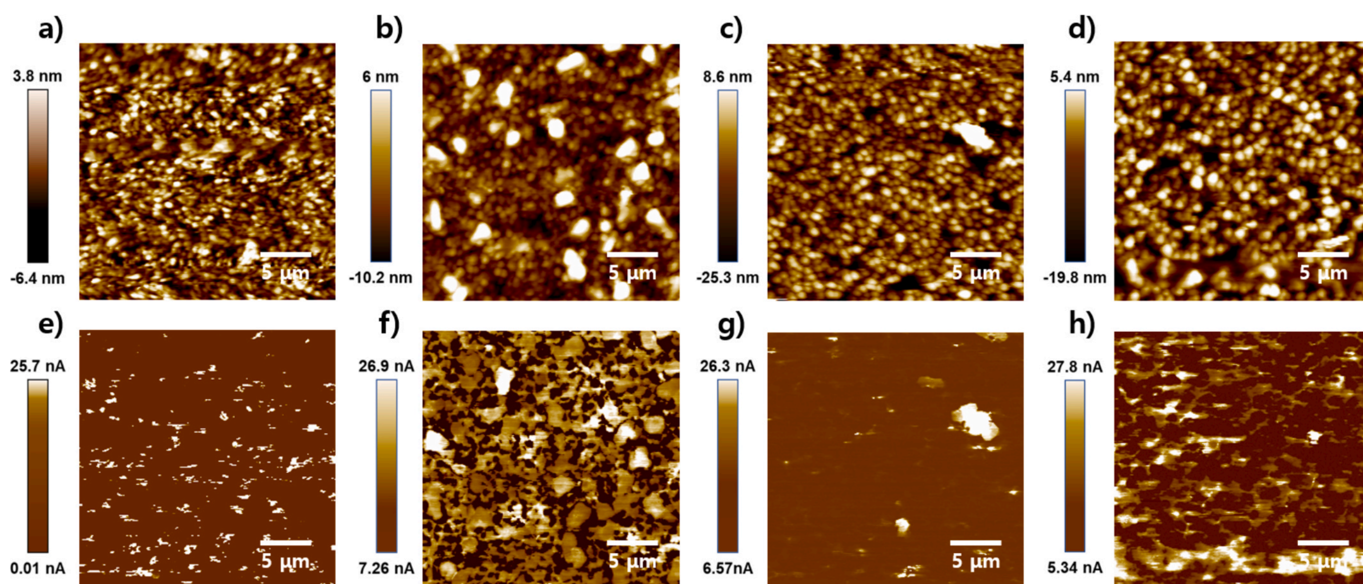

Fig. 5. A-d) z heights and e-h) conductive afm topography images of se 0–30 W/TeO_x active film samples.

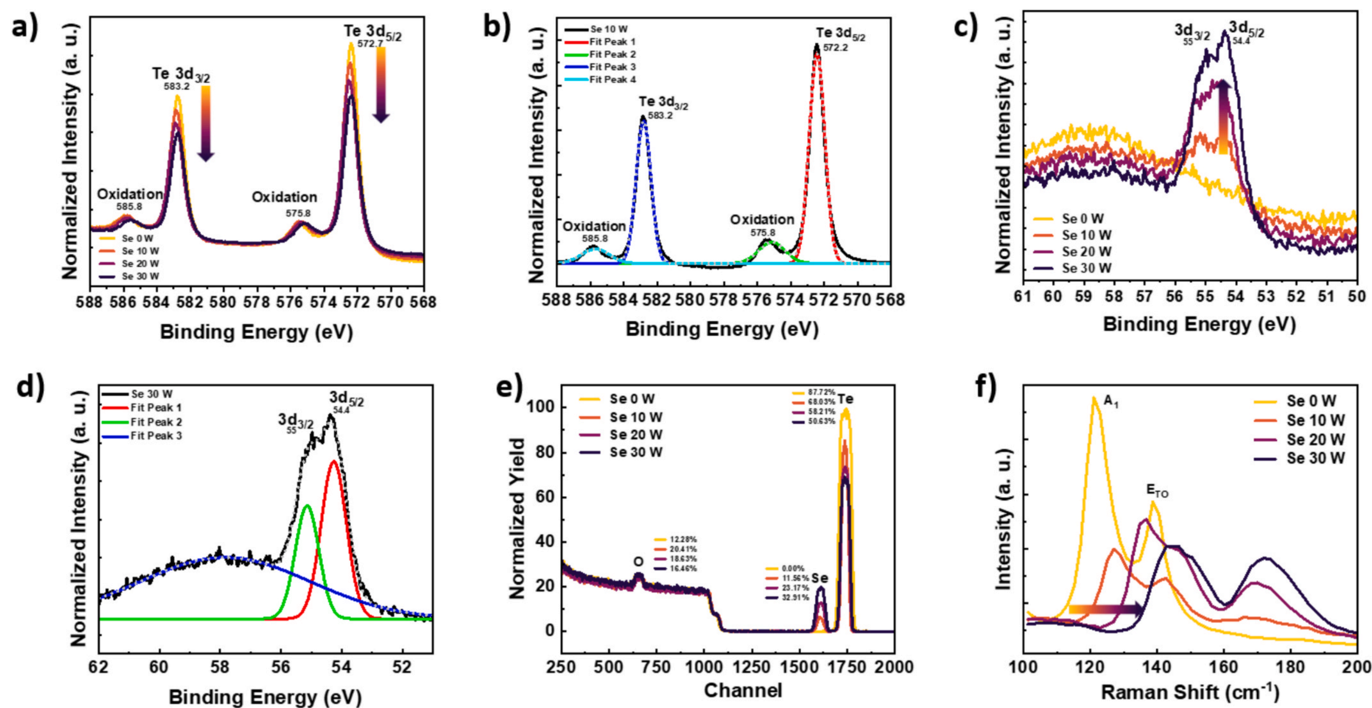

Fig. 6. A) a comprehensive Te and c) Se XPS spectrum set of active-layer deposition conditions and b) single XPS graph of the Se 10 W or d) 30 W/TeO_x condition active-layer. e) RBS data and f) Raman spectra of Se-alloyed TeO_x film samples.

Table 1
Areal density and composition ratio according to the active-layer deposition conditions.

Active-Layer	Areal Density (atoms/cm^2)	Atomic Percent Ratio
Se 0 W / TeO_x	3.70×10^{17}	$Te_{0.82}O_{0.18}$
Se 10 W / TeO_x	2.40×10^{17}	$Se_{0.12}Te_{0.72}$ $O_{0.16}$ // 1: 6
Se 20 W / TeO_x	2.90×10^{17}	$Se_{0.24}Te_{0.60}O_{0.16}$ // 1: 2.5
Se 30 W / TeO_x	3.40×10^{17}	$Se_{0.34}Te_{0.52}O_{0.14}$ // 1: 1.53

electrode-dependent operation of the oxidized OTS selector device. Subsequently, a second hypothesis can be established, which describes the Schottky junction caused by the difference between the work function of the electrode and the Fermi level of each active-layer condition—specifically, the limitation at the interface. To investigate this, the energy levels of the four active-layer conditions used in this study were determined through optical characterization. The absorbance and the corresponding tauc plots were analyzed to estimate the shape and magnitude of the bandgap and the positions of the valence band and conduction band were identified through ultraviolet photoelectron spectroscopy (UPS) measurements[47].

As shown in Fig. S5 (Supporting Information), the absorption region gradually decreases as the Se content is increased. This likely indicates

an increase in the bandgap due to the incorporation of Se into the lattice structure [48], and this assumption is substantiated by the tauc plot in Fig. 7a [49]. The band transition index for all four conditions was calculated and found to be 1/2, and the estimated bandgap values were 1.52, 1.64, 2.00 and 2.28 eV for each condition [50]. Furthermore, a UPS analysis was conducted to obtain more detailed band structure information [51]. As shown in Fig. 7b, the work function and E_{ff}–E_v values for the four active-layer conditions were derived from the measurement results, and the full dataset is summarized in Table 2 [52]. The thin films under these four active-layer conditions are all p-type films fabricated by the co-sputtering of Se and Te, according to Fig. S6 (Supporting Information), XRD measurements confirm that they are amorphous [53].

Fig. 7c illustrates the interfacial energy alignment between the electrode and each active-layer condition, demonstrating that Pt, W, Cr and Ni form ohmic contacts, whereas Ti and Al form Schottky contacts [54].

However, this hypothesis cannot provide a full explanation of the device characteristics, as it cannot account for the non-functionality of the Se 0 W condition, nor the failure of the Ni electrode device—despite the presence of an ohmic junction—to operate as a selector, in contrast to other functional electrode configurations.

3.2.3. *Hypothesis 3: Effects of interfacial defects between active-layer and electrode*

In Chapter 3.2.2, instead of focusing on bulk-limited conduction, we considered that interfacial constraints between the electrode and active-layer were more dominant. However, this behavior could not be fully explained by the band alignment alone. Other interfacial factors—such as oxidation or surface roughness—rather than the intrinsic material properties, may influence selector performance outcomes. To verify this, we analyzed the device cross-section using scanning electron microscopy (SEM) and characterized the interface using TEM and EELS. SEM was used to check for structural issues at the interface, while TEM/EDS/EELS identified interfacial defects.

The SEM analysis confirms an acceptable structure for most electrodes (Fig. 8), though Cr exhibited non-uniform film growth. In contrast, the metal film quality of the Ni and Al electrodes was poor and these samples showed severely damaged interfaces.

As a further check for interfacial defects, cross-sectional TEM images were obtained for each electrode. As shown in Fig. 9a–f, no clear oxide layers were observed in the Pt, W and Cr electrodes, whereas Ti, Ni and Al showed visible interfacial oxide layers. This observation was supported by EDS mapping (Fig. 9g–l), where the oxygen intensity was higher in the Ti, Ni and Al cases, confirming oxidation of the electrode.

An EELS analysis, which provides elemental information by detecting the energy loss of electrons interacting with specific atoms in the sample, offers a higher spatial resolution for atomic distribution compared to EDS [55]. The corresponding EELS results were obtained along the directions indicated by the arrows shown in Fig. 9a–f. As shown in Fig. 10a–c, no significant oxygen signal was found at the interface, in contrast, as shown Fig. 10d–f, the presence of oxygen was strongly detected. In particular, the Al electrode exhibited an oxide layer approximately 10 nm thick, explaining the poor electrical performance of the selector in this case (Fig. 10f). In this work, electrode-induced interfacial oxidation refers to a degradation mechanism where the electrode scavenges oxygen from the active layer. This oxygen depletion leaves unpassivated Te/Se dangling bonds, which subsequently reform the continuous metallic Te-Te network. As summarized by the Raman spectroscopy analysis in Fig. S7, the presence of oxygen suppresses the metallic Te–Te bonding, whereas its absence leads to the recovery of the Te–Te network. Consequently, these interfacial defects facilitate uncontrollable percolative Ohmic conduction, ultimately eliminating the threshold switching behavior.

Pt and W electrodes are known to exhibit minimal oxidation, while Cr forms Cr_2O_3, which suppresses oxygen diffusion and serves as a passivation layer [56], thereby enhancing the stability of the interface. In contrast, Ni, Ti and Al form insulating oxides that function as interfacial defects, impeding the current flow of current. These results support the initial hypothesis that oxidation-induced interfacial defects significantly impact selector performance. Oxygen-related interface defects were found to strongly influence charge transport.

Table 2
Material properties of each deposition condition.

Active-Layer Condition	Bandgap Energy (E_g / eV)	Work Function (eV)	$E_f - E_v$ (eV)
Se 0 W / TeO_x	1.52	4.28	0.56
Se 10 W / TeO_x	1.64	4.10	0.39
Se 20 W / TeO_x	2.00	4.45	0.43
Se 30 W / TeO_x	2.28	4.46	0.53

4. Conclusions

In this study, we investigated selector operation in intentionally oxidized chalcogenide OTS materials using a via-hole device platform. A modest O_2 flow during active-layer deposition was not a parasitic artifact but an engineering knob that tailors the interfacial defect spectrum and band alignment. This control enabled sub-1 V threshold ($V_{th} \approx 0.78$ V) and high selectivity ($>10^4$) under a Pt top electrode—figures that are difficult to reach with oxygen-free SeTe-based layers under identical processing.

To elucidate the mechanism behind the electrode-dependent behavior, we tested three hypotheses. First, Hypothesis 1 (Bulk-limited conduction) posits that the switching is determined by the intrinsic properties of the Se-alloyed TeO_x layer. However, this hypothesis conflicts with our experimental observation that the device performance

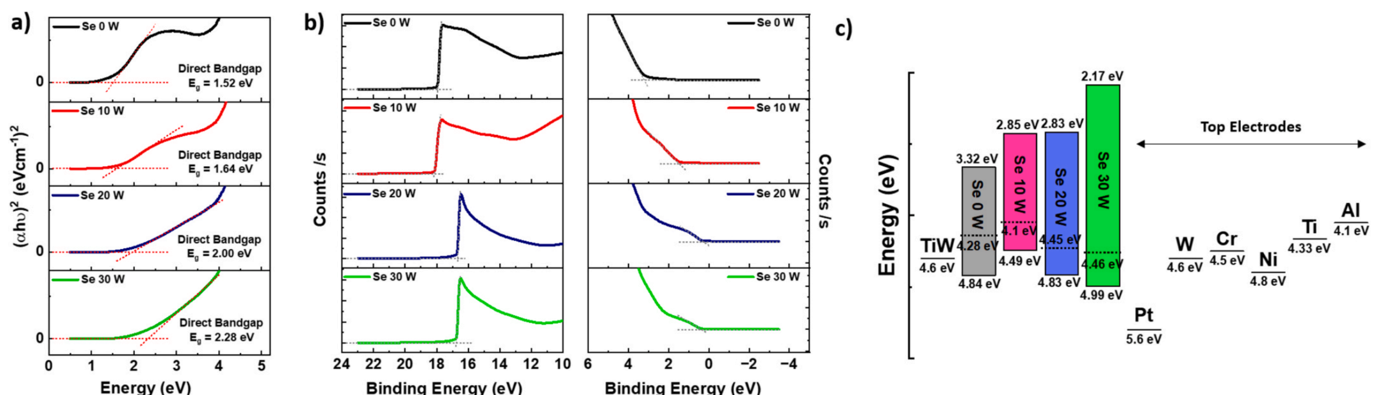

Fig. 7. A) tauc plot, b) ups spectra near the conduction or valance band and c) band alignment of se-alloyed teo_x films based on absorbance and UPS data.

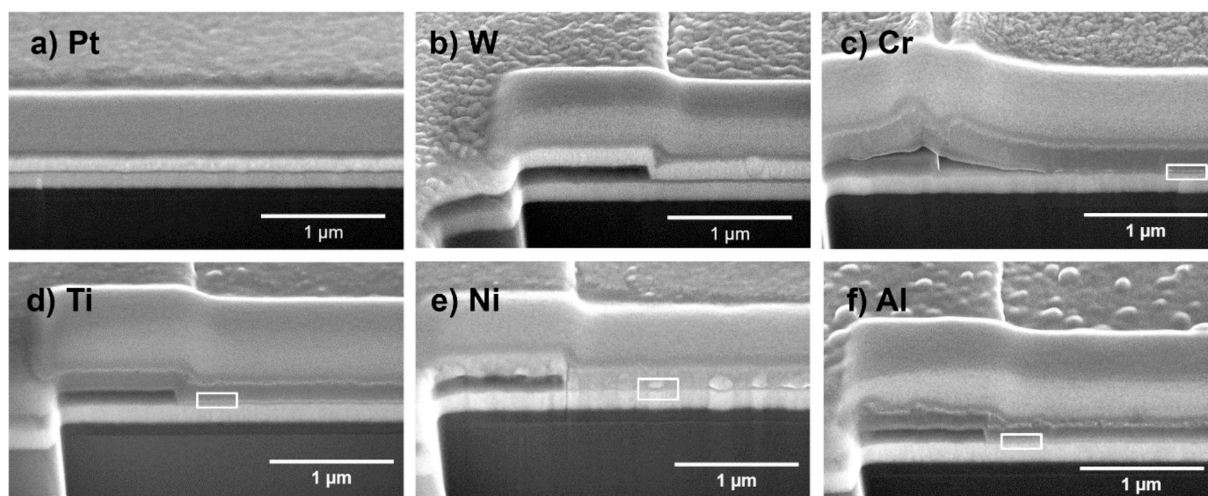

Fig. 8. Selector device cross-sectional FIB-SEM images with a) Pt, b) W, c) Cr, d) Ti, e) Ni and f) Al electrodes for structural and defect identification.

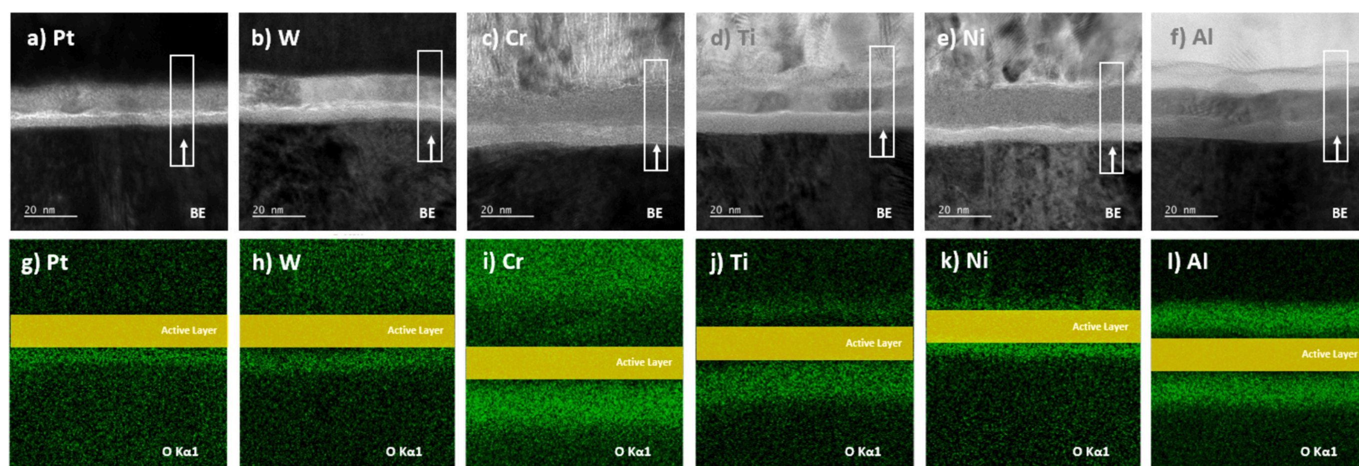

Fig. 9. A-f) active-layer stem images between top and bottom electrodes and g-i) oxygen kα1 intensity eds images for each top electrode condition.

varies significantly depending on the electrode material. If the mechanism were purely bulk-controlled, the electrode influence should be negligible. This discrepancy compels us to rule out Hypothesis 1 as the primary driver and focus on the interface properties (Hypotheses 2 and 3).

Next, regarding the interface, Hypothesis 2 (Work function mismatch) suggests that a high Schottky barrier is the cause of the issue. While this explains the initial high resistance, it fails to account for the irreversible degradation observed in specific electrode combinations. This indicates that a purely physical model (Hypothesis 2) is insufficient.

This logical limitation leads us to Hypothesis 3 (Interfacial oxidation). Our analysis reveals that the oxidation of the electrode by the oxide active layer creates an unexpected insulating layer. Interestingly, this chemical reaction (Hypothesis 3) is closely associated with Hypothesis 2, as it physically modifies the effective barrier height and width, making the actual contact resistance much higher than theoretically predicted by the work function difference alone. Therefore, we conclude that Hypothesis 3 is the governing mechanism, as it provides the root cause for the interface instability that Hypothesis 1 and 2 could not fully explain.

These results articulate the advantage of oxidized OTS: when oxygen is introduced deliberately and within a narrow process window, it (i) suppresses filamentary/irreversible paths, (ii) increases subthreshold nonlinearity by defect/field engineering, and (iii) permits low-voltage, reproducible operation compatible with BEOL constraints. Importantly, the role of the electrode is not merely incidental; it co-defines the interfacial oxidation state and thus must be co-optimized with oxygen incorporation.

While the present work establishes a materials-agnostic guideline—"controlled interfacial oxidation + appropriate electrode choice"—we recognize the value of generality checks in canonical OTS chemistries (e.g., Ge–As–Se). Extending the same via-hole methodology and interfacial analyses to those systems constitutes a clear avenue for future work and will further delineate which aspects are universal versus composition-specific.

Overall, our findings convert "oxidation risk" into a design parameter for selector integration: by co-tuning oxygen incorporation and the electrode, oxidized chalcogenide OTS selectors achieve low V_{th} (Fig. S8, Supporting Information), high selectivity and reproducible switching needed for next-generation 3D cross-point arrays.

CRediT authorship contribution statement

MiRiNae Lee: Writing – review & editing, Writing – original draft, Investigation, Formal analysis, Data curation. **Jung Hoon Han:** Writing – review & editing, Investigation, Formal analysis. **Chahwan Yang:** Writing – review & editing, Investigation, Formal analysis. **Kyunghee Choi:** Writing – review & editing, Supervision, Investigation, Conceptualization. **Sooji Nam:** Writing – review & editing, Writing – original draft, Supervision, Investigation, Conceptualization.

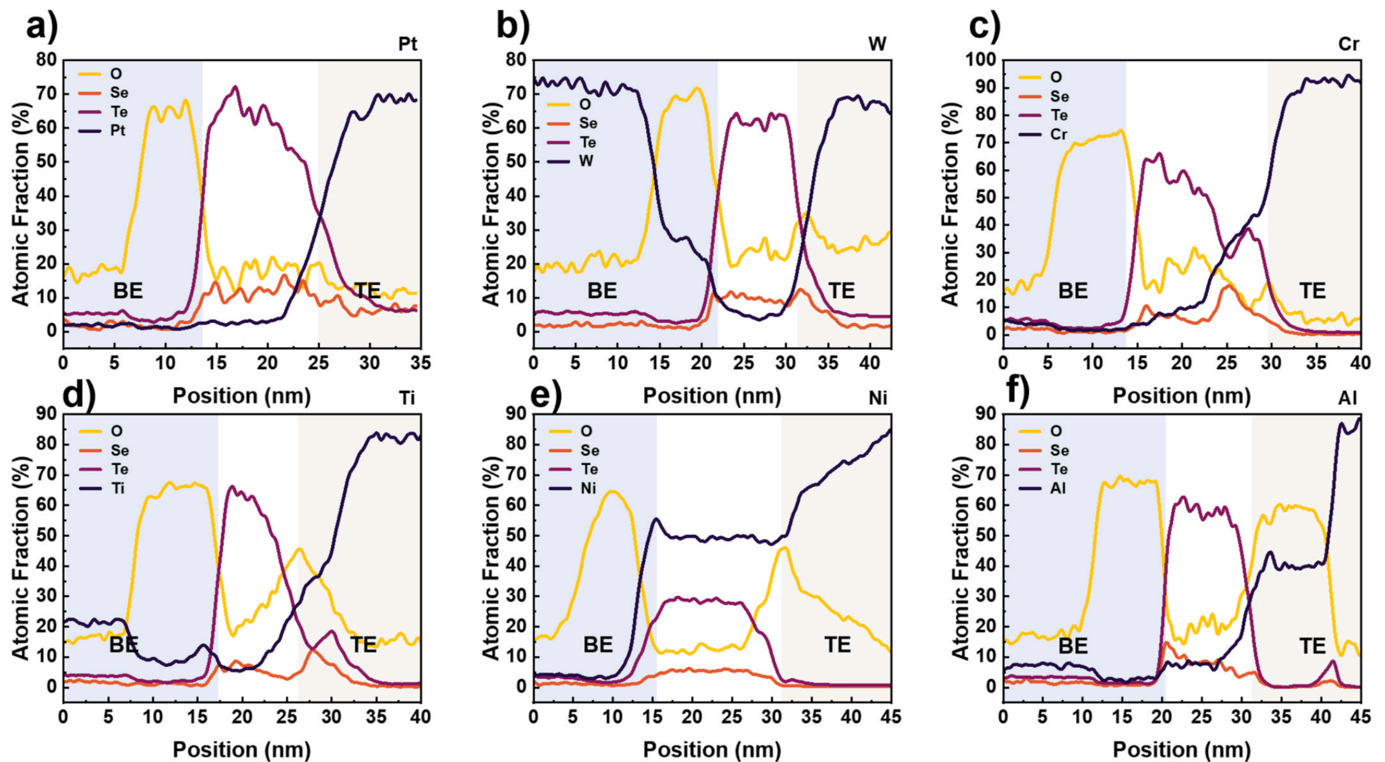

Fig. 10. Line scanning EELS graph for identifying oxidation defects at the interface for a) Pt, b) W, c) Cr, d) Ti, e) Ni and f) Al electrodes.

Declaration of competing interest

The authors declare that they have no known competing financial interests or personal relationships that could have appeared to influence the work reported in this paper.

Acknowledgments

This work was supported by the Technology Innovation Program(or Industrial Strategic Technology Development Program(RS-2025-02308064) funded By the Ministry of Trade Industry & Energy(MOTIE, Korea), and was supported internal fund/grant of Electronics and Telecommunications Research Institute (ETRI)[25YC1400 and 25YC1500].

Appendix A. Supplementary data

Supplementary data to this article can be found online at https://doi.org/10.1016/j.apsusc.2026.166674.

Data availability

Data will be made available on request.

References

[1] Strubell, Emma, Ananya Ganesh, and Andrew McCallum. Proceedings of the AAAI conference on artificial intelligence. Vol. 34. No. 09. 2020.
[2] Rydning, David Reinsel-John Gantz-John, John Reinsel, and John Gantz. Framingham: International Data Corporation 16 (2018): 1-28.
[3] Patel, Dylan, Daniel Nishball, and Jeremie Eliahou Ontiveros. SemiAnalysis, March 13 (2024).
[4] J. Koomey, A report by Analytical Press, completed at the request of the, N.Y. Times 9 (2011) (2011) 161.
[5] E. Masanet, et al., Science 367 (6481) (2020) 984–986.
[6] E. Masanet, N. Lei, Aspen Global Change Institute (2020).
[7] E. Pop, Nano Res. 3 (3) (2010) 147–169.
[8] F. Tavakkoli, et al., Int. J. Heat Mass Transf. 97 (2016) 337–352.
[9] W. Wondrak, Microelectron. Reliab. 39 (6-7) (1999) 1113–1120.
[10] J.D. Meindl, Q. Chen, J.A. Davis, Science 293 (5537) (2001) 2044–2049.
[11] Vashchenko, Vladislav A., and Vladimir F. Boston, MA: Springer US, 2008.
[12] L.T. Su, et al., IEEE Trans. Electron Devices 41 (1) (2002) 69–75.
[13] Keyes, Robert W. Proceedings of the IEEE 89.3 (2002): 227-239.
[14] Pop, Eric, Robert Dutton, and Kenneth Goodson. IEEE International Electron Devices Meeting 2003. IEEE, 2003.
[15] R. Rhyner, M. Luisier, Nano Lett. 16 (2) (2016) 1022–1026.
[16] Z. Zhao, et al., Nano-Micro Letters 16 (1) (2024) 81.
[17] S. Ban, et al., Adv. Electron. Mater. 11 (6) (2025) 2400665.
[18] Lanza, Mario, ed. John Wiley & Sons, 2017.
[19] E. Ambrosi, C.-H. Wu, H.-Y. Lee, C.-M. Lee, C.-F. Hsu, et al., IEEE Electron Device Lett. 43 (2022) 1673–1676.
[20] E. Ambrosi, C.H. Wu, H.Y. Lee, P.C. Chang, C.F. Hsu et al., in 2021 IEEE International Electron Devices Meeting (IEDM). San Francisco, CA, USA. 28.5.1–28.5.4 (2021).
[21] M.J. Lee, D. Lee, S.H. Cho, J.H. Hur, S.M. Lee, et al., Nat. Commun. 4 (2013) 2629.
[22] H.Y. Cheng, W.C. Chien, I.T. Kuo, E.K. Lai, Y. Zhu et al., in 2017 IEEE International Electron Devices Meeting (IEDM). San Francisco, CA, USA. 2.2.1–2.2.4 (2017).
[23] L. Zhu, et al., J. Mater. Chem. C 5 (14) (2017) 3592–3599.
[24] X. Zhou, et al., Sci. Rep. 5 (1) (2015) 11150.
[25] Cheng, H. Y., et al. 2018 IEEE International Electron Devices Meeting (IEDM). IEEE, 2018.
[26] S. Hatayama, et al., ACS Appl. Electron. Mater. 7 (6) (2025) 2650–2659.
[27] R. Waser, et al., Advanced Materials (Deerfield Beach, Fla.) 21 (25-26) (2009) 2632–2663.
[28] H.C. Lin, P.D. Ye, G.D. Wilk, Appl. Phys. Lett. 87 (2005) 18.
[29] M. Kazemi, et al., J. Clust. Sci. 30 (2019) 767–775.
[30] M.A. Lampert, Phys. Rev. 103 (6) (1956) 1648.
[31] Sze, Simon M., Yiming Li, and Kwok K. Ng. John Wiley & sons, 2021.
[32] A. Rose, Space-charge-limited currents in solids, Phys. Rev. 97 (6) (1955) 1538.
[33] J. Frenkel, Phys. Rev. 54 (8) (1938) 647.
[34] J.G. Simmons, J. Appl. Phys. 34 (6) (1963) 1793–1803.
[35] F.A. Padovani, R. Stratton, Solid State Electron. 9 (7) (1966) 695–707.
[36] R.T. Tung, Phys. Rev. B 45 (23) (1992) 13509.
[37] C. Jeynes, N.P. Barradas, E. Szilágyi, Anal. Chem. 84 (14) (2012) 6061–6069.
[38] N.P. Barradas, J. Phys. D Appl. Phys. 34 (14) (2001) 2109.
[39] J. Matthew, Surf. Interface Anal. 36 (13) (2004) 1647.
[40] J.F. Watts, S. Science, Techniques 45 (1994) 5.
[41] F. Giannazzo, et al., Nanomaterials 10 (4) (2020) 803.
[42] T.W. Kelley, E. Granstrom, and C, Daniel Frisbie. Advanced Materials 11 (3) (1999) 261–264.
[43] Almeida, et al., J. Non-Cryst. Solids 353 (2007) 2066.
[44] Kim, et al., AIP Adv. 13 (2023) 035221.
[45] B.V.R. Chowdari, and P, Pramoda Kumari. Solid State Ionics 113 (1998) 665–675.
[46] Pine, A. S., and G. J. P. R. B. Dresselhaus. Physical Review B 4.2 (1971): 356.
[47] J. Tauc, Mater. Res. Bull. 3 (1) (1968) 37–46.
[48] M. Wuttig, N. Yamada, Nat. Mater. 6 (11) (2007) 824–832.

[49] Daniels, J., et al. Springer Tracts in Modern Physics, Volume 54. Berlin, Heidelberg: Springer Berlin Heidelberg, 2006. 77-135.
[50] J. Shi, et al., Adv. Mater. 33 (50) (2021) 2006230.
[51] Hüfner, Stephan. Springer Science & Business Media, 2013.
[52] Sze, Simon M., Yiming Li, and Kwok K. Ng. John Wiley & Sons, 2021.
[53] Rhoderick, Emlyn Huw. IEE Proceedings I (Solid-State and Electron Devices) 129.1 (1982): 1-14.
[54] R.T. Tung, Appl. Phys. Rev. 1 (2014) 1.
[55] Egerton, Ray F. Springer Science & Business Media, 2011.
[56] M. Weiser, et al., NPJ Mater. Degrad. 7 (1) (2023) 70.